ACS APPLIED MATERIALS & INTERFACES

Research Article

www.acsami.org

Colloidal Solution-Processed $CuInSe_2$ Solar Cells with Significantly Improved Efficiency up to 9% by Morphological Improvement

Ye Seul Lim,[†,‡] Hyung-Soon Kwon,[§] Jeunghyun Jeong,[†] Jin Young Kim,[†] Honggon Kim,[†] Min Jae Ko,[†] Unyong Jeong,[‡] and Doh-Kwon Lee*[,†]

[†]Photo-electronic Hybrids Research Center, Korea Institute of Science and Technology (KIST), Seoul 136-791, Korea

[‡]Department of Materials Science and Engineering, Yonsei University, Seoul 120-749, Korea

[§]Department of Materials Science and Engineering, Seoul National University, Seoul 151-742, Korea

Supporting Information

ABSTRACT: We demonstrate here that an improvement in the green density leads to a great enhancement in the photovoltaic performance of $CuInSe_2$ (CISe) solar cells fabricated with Cu−In nanoparticle precursor films via colloidal solution deposition. Cold-isostatic pressing (CIP) increases the precursor film density by ca. 20%, which results in an appreciable improvement in the microstructural features of the sintered CISe film in terms of a lower porosity, a more uniform surface morphology, and a thinner $MoSe_2$ layer. The low-band-gap (1.0 eV) CISe solar cells with the CIP-treated films exhibit greatly enhanced open-circuit voltage (V_{OC}, typically from 0.265 to 0.413 V) and fill factor (FF, typically from 0.34 to 0.55), compared to the control devices. As a consequence, an almost 3-fold increase in the average efficiency, from 3.0 to 8.2% (with the highest value of 9.02%), is realized. Diode analysis reveals that the enhanced V_{OC} and FF are essentially attributed to the reduced reverse saturation current density and diode ideality factor. This is associated with suppressed recombination, likely due to the reduction in recombination sites at grain/air surfaces, intergranular interfaces, and defective CISe/CdS junctions. From the temperature dependences of V_{OC}, it is revealed that CIP-treated devices suffer less from interface recombination.

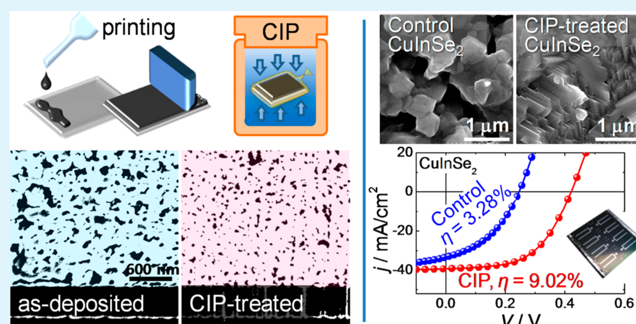

KEYWORDS: *$CuInSe_2$, thin-film solar cells, Cu−In, nanoparticles, packing density, cold-isostatic pressing*

1. INTRODUCTION

A nonvacuum process for thin-film fabrication employing either a colloidal solution precursor (also called ink, suspension, or slurry) or a chemical solution precursor has been attracting a lot of attention as an appealing alternative to the vacuum deposition techniques because of its cost-effectiveness and scalability.[1,2] In recent years, immense efforts have been made to apply the nonvacuum, solution deposition methods in order to realize low-cost optoelectronic and electrochemical devices such as thin-film solar cells,[3,4] quantum-dot solar cells,[5] transparent conducting oxide electrodes,[6] superconductor films,[7] and solid oxide fuel cells,[8] to name a few. Among various thin-film photovoltaic (PV) cells, nonvacuum deposition techniques have been applied most extensively to I−III−VI_2 compound-based solar cells. Chalcopyrite $CuInSe_2$ (CISe) is a direct-band-gap semiconductor boasting a high absorption coefficient (∼10^5 cm^{-1}) and has excellent material stability including exceptional radiation hardness.[9] In addition, its band-gap energy, E_g, can be tuned to range from 1.0 eV (CISe) to 2.4 eV ($CuGaS_2$), by substituting Ga and S for In and Se, respectively. To date, a power conversion efficiency (PCE) as high as 20.4% has been demonstrated for PV cells with $Cu_{0.8}(In_{0.65}Ga_{0.35})Se_2$ (CIGSe), which has E_g = 1.2 eV.[10] Such an outstanding PV performance, which is comparable to that of polycrystalline Si solar cells, and the excellent outdoor stability of state-of-the-art CIGSe PV cells could be realized using vacuum-based deposition techniques such as multistage coevaporation and sputtering; however, the high production costs and difficulties in scaling-up these vacuum deposition techniques have provoked a great deal of interest in the development of nonvacuum deposition processes that have the potential for high-throughput production of low-cost PV devices.[11]

Nonvacuum deposition processes used for the fabrication of CIGSe-based solar cells could be classified into two methods: electrochemical deposition (ED) and solution deposition. The ED technique results in a highly dense precursor film, but it requires a longer deposition time and suffers from difficulty in controlling the composition of the film.[12,13] The latter often requires replenishment of In and Ga in the as-electrodeposited

Received: September 23, 2013
Accepted: December 11, 2013
Published: December 11, 2013

ACS Publications © 2013 American Chemical Society

film by physical vapor deposition, requires the formation of a multilayer precursor film by ED, or requires etching of the Cu-excess phases in the CISe film using a toxic KCN solution,[14] to adjust the overall composition into a Cu-deficient regime. On the other hand, the solution deposition process offers advantages such as a good controllability of the film composition over a large area and a rapid deposition time.[15] Solution deposition can be carried out with a colloidal solution precursor,[15−22] a chemical solution precursor,[23−30] or with a composite of both,[8,31−33] by utilizing a variety of nonvacuum deposition techniques, depending on the rheological properties of precursors, such as spray deposition, spin coating, dip coating, printing, and electrospinning.

The chemical solution precursor route has been most successfully demonstrated by Mitzi et al., who achieved a PCE as high as 15.2% using a hydrazine solution containing metal chalcogenides and elemental chalcogens.[23] However, the widespread use of this method is hampered because of the highly toxic and explosive nature of hydrazine. Consequently, more solution precursor routes were developed that employ nontoxic solvents such as water and alcohol, along with organic binders as a rheology modifier. However, the incomplete decomposition of these organic additives during annealing under an oxygen-free atmosphere often led to the formation of a thick carbon layer in the annealed film,[24,32] which acts as a barrier against charge collection. Additional oxidation is thus required to totally burn the organic substances.[26,27] This step may add complexity to an otherwise simple process. On the other hand, by employing colloidal precursor routes, Norsworthy et al. demonstrated a 10.5% efficiency for the CISe solar cell, which was achieved by selenization of the Cu−In alloy precursor film with H_2Se gas.[17] Despite such a promising efficiency, the use of $H_2Se(g)$ has not been considered to be favorable for commercialization because of its high toxicity.[30] Recently, however, Hillhouse et al. used a less toxic Se vapor and reported a 12% efficiency for Cu(In,Ga)-$(S,Se)_2$ PV devices fabricated using Cu(In,Ga)S_2 nanocrystal ink along with Na doping.[15] Although this approach put forth an environmentally friendly process using a colloidal precursor, it still had similar drawbacks, namely, etching with toxic KCN and a preannealing to remove organic materials. Jeong et al. employed a CISe nanoparticle suspension, where the excess CuSe phase was also present as a sintering agent, and obtained a PCE of 8.2%,[22] which was among the highest efficiencies for a low-band-gap CISe device fabricated by solution deposition methods without using toxic solvents or gases. It should be noted, however, that the CISe films used in their work were not only selenized in a vacuum evaporator but also suffered from carbon contamination.

In our earlier work,[34] we presented a facile colloidal precursor route for CISe solar cells using Cu−In alloy nanoparticles, which consisted of Cu_2In (ca. 15 nm in size), CuIn (40−100 nm), and amorphous In, to fabricate low-band-gap CISe as a model system and a promising candidate for the bottom cell in a prospective tandem structure. The use of a metallic precursor enables one to utilize the huge volume expansion associated with phase transformation into selenides in densification of the thin film. By using the intermetallic compound mixture, the overall composition of the film could be controlled in the Cu-deficient regime, alleviating the need for etching with a KCN solution to remove undesired Cu_xSe phases.[21] Ball milling was employed to prepare the colloidal precursor in ethanol. No organic substances such as surfactants, binders, or dispersants were added, thus yielding almost C-free CISe films without an additional oxidation step.[34] The entire process for the fabrication of CISe films, including nanoparticle synthesis, thin-film deposition, and reactive annealing under a Se(g)-containing atmosphere, was carried out under ambient conditions at atmospheric pressure.

In this work, a particular emphasis is placed on the effect of "green density" (precursor film density) on the microstructure of sintered CISe films and the resulting PV performances. The microstructure of a CISe-based thin film, together with its composition are the most critical material properties influencing the device performances. A low packing density of the precursor film may inhibit densification of the film, leaving many pores inside, and often increase the surface roughness of the sintered film. Moreover, a Se vapor may easily permeate through the highly porous precursor layer, resulting in the formation of a thick $MoSe_2$ layer. Those structural imperfections induce high recombination, shunt conductance, and series resistance in the resulting devices. In spite of its significance, however, the effect of the precursor film density has not been extensively explored. Although organic additives usually improve the morphology of the precursor layer, they can leave C residue in the sintered films. The idea of physical pressing has been presented by Eldada et al. in their reactive-transfer method.[35] However, the effect of the precursor film density on the device performance was not explicitly elucidated because a mechanical pressure was applied during reactive annealing and an electric field was simultaneously applied. Herein, we demonstrate that an improved green density by cold-isostatic pressing (CIP) resulted in a better microstructural development of CISe films. As a consequence, a remarkable improvement was achieved in the open-circuit voltage (V_{OC}) and fill factor (FF) of the CISe PV cells. On the basis of a comparative analysis of the diode characteristics of CISe devices with and without CIP treatment, the origin of the enhanced values of V_{OC} and FF, which are typically observed to be lower in wet-processed CIGSe solar cells, was discussed.

2. EXPERIMENTAL SECTION

Formation of a Colloidal Solution of Cu−In Alloy Nanoparticles. Cu−In intermetallic nanoparticles were synthesized via a chemical reduction method under ambient conditions.[34,36] A precursor solution was prepared by dissolving copper(II) chloride (5.56 mM , Aldrich, 99.999%) and indium(III) chloride (6.95 mM, Aldrich, 99.999%) in tetraethylene glycol (TEG; 50 mL, Aldrich, 99%). The atomic ratio of copper to indium in the solution was 0.8. A reducing solution was formed by dissolving sodium borohydride ($NaBH_4$; 75 mM, Junsei, 98%) in TEG (50 mL). Thereafter, the precursor solution was added at a rate of 1 mL min^{-1} into the reducing solution that was kept at 0 °C, yielding black precipitates (Figure S1 in the Supporting Information, SI; see also ref 34 for a detailed analysis of the as-synthesized nanoparticles). A colloidal solution precursor for printing was prepared by dispersing the as-synthesized nanoparticles (4 g) in anhydrous ethanol (25 mL). Then, the solution was ball-milled at 200 rpm using 1- and 5-mm-diameter ZrO_2 balls in a ratio of 7:3. To examine the effect of the precursor film density more clearly, milling was carried out for a shorter period of time, e.g., 24 h, in comparison with the previous work (more than 72 h).[34] No organic dispersant or binder was added in the colloidal solution precursor.

Solar Cell Fabrication. The experimental procedure for fabricating CISe solar cells by using colloidal precursor deposition and CIP is schematically illustrated in Figure 1. The colloidal solution precursor was doctor-blade-coated to produce Cu−In alloy precursor films on Mo-sputtered soda-lime glass substrates ($30 \times 40 \times 1$ mm^3). In order to investigate the influence of the porosity of precursor films,

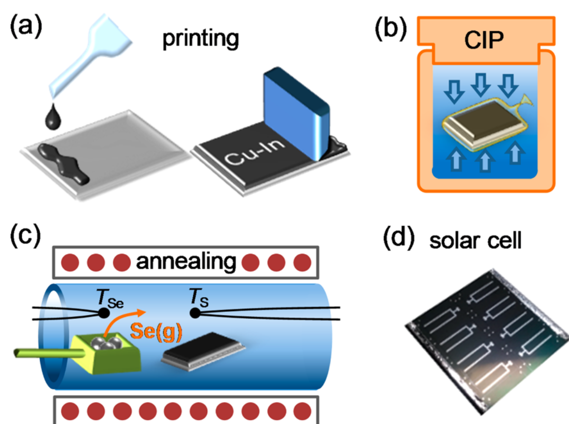

Figure 1. Schematic of the processing route for CISe thin-film solar cells: (a) printing Cu−In alloy nanoparticle film; (b) CIP; (c) reactive annealing; (d) solar cell fabrication.

CIP was conducted at 250 MPa for 5 min (Flow Autoclave Systems Inc., USA). Uniaxial pressing (see Figure S2 in the SI) was found to be less effective to get uniformly compressed films. Reactive annealing of the precursor films was carried out in a Se-containing gas atmosphere at atmospheric pressure. Selenium pellets (0.2 g, 99.99%, Aldrich) were used with an Ar carrier gas (at a flow rate of 100 sccm) as a Se source. The precursor films were preannealed at 300 °C for 30 min, subsequently heated up to 500 °C at a rate of 10 °C min^{-1}, and annealed for 30 min before being furnace-cooled. At the annealing temperature of the thin film (500 °C), the Se source was placed at about 350 °C, which yields a Se partial pressure of 1.6×10^{-3} atm.[34,37] Solar cells were fabricated in a conventional configuration, Mo/CISe/CdS/i-ZnO/AZO/Al, where i-ZnO is intrinsic ZnO and AZO is Al-doped ZnO. A CdS buffer layer (ca. 70 nm in thickness) was deposited on the CISe film via chemical bath deposition with a solution containing $CdSO_4$ (2 mM), NH_4OH (1.02 M), and thiourea (84 mM) at 60 °C for 20 min. The i-ZnO (50 nm) and AZO (620 nm) layers were deposited onto the CdS layer using radio-frequency magnetron sputtering. A Ni/Al grid (50 nm/500 nm) was deposited as a current collector by electron beam evaporation onto the ZnO layer, with the remaining surface acting as an active area measuring 0.3−0.4 cm^2.

Characterization of Thin Films and PV Devices. The surface and cross-sectional morphologies of the precursor and selenized films were characterized using field-emission scanning electron microscopy (FE-SEM) at an acceleration voltage of 15 kV, and their compositions were analyzed by energy-dispersive X-ray spectrometry (EDS) at an acceleration voltage of 20 kV with an acquisition time of 60 s (Hitachi, S-4200). The EDS spectra were collected from at least five randomly selected areas over an entire sample surface. The compositions of thin films were confirmed with electron probe X-ray microanalysis at an acceleration voltage of 20 kV with a beam spot radius of 30 μm (JEOL, JXA-8500F) by measuring five times. The crystal structures of the precursor and selenized films were investigated using X-ray diffraction (XRD; Rigaku, D/max 2500) with Cu Kα radiation (λ = 0.15418 nm). Raman spectra of the selenized films were recorded with a Renishaw inVia spectrometer equipped with a 50 mW, 532-nm-wavelength, Ar$^+$-laser excitation beam. The relative atomic concentration profiles across the thicknesses of the selenized films were examined by Auger electron spectroscopy (AES; Scanning Auger Nanoprobe PHI-700 & LC-TOFMS LECO) with ion-beam sputtering. The photocurrent−voltage (j−V) characteristics of the solar cells were investigated using a class-AAA solar simulator (Yamashita Denso, YSS-50S) equipped with a 180 W Xe lamp and an AM 1.5G filter (ASTM E927-05, IEC 60904-9). The light intensity was adjusted with an NREL-calibrated Si solar cell to approximate 1 sun of light intensity (100 mW cm^{-2}). External quantum efficiencies (EQEs) were measured under short-circuit conditions using an incident photon-to-current conversion efficiency measurement system equipped with a 75 W Xe lamp and a grating monochromator (PV Measurements, Inc.). A calibration was carried out using a Si photodiode (G425) in the spectral range from 300 to 1000 nm and a Ge photodiode from 900 to 1400 nm. Both photodiodes had standard NIST calibration.

3. RESULTS

Figure 2 shows the XRD pattern, typical surface morphologies, and cross sections for the as-deposited film and the film with an

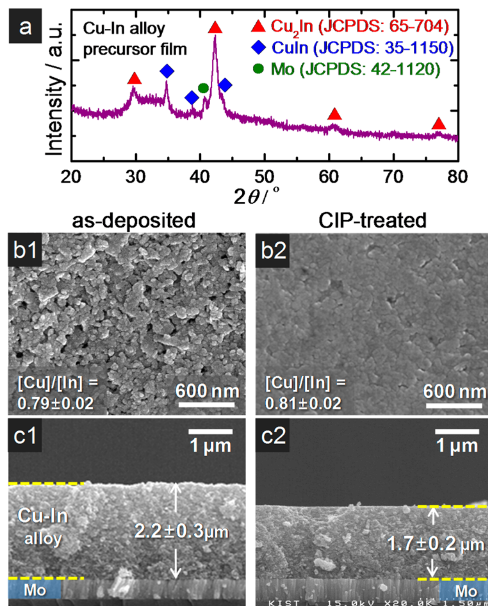

Figure 2. (a) XRD pattern and (b and c) typical SEM images of the precursor films based on Cu−In intermetallic nanoparticles for the as-deposited film (left) and CIP-treated film (right). (b) Film surfaces and (c) cross sections.

improved packing density by CIP. It is noted that the amorphous nature of the XRD pattern for the as-deposited film can be attributed to the post-synthesis process, i.e., ball milling.[34] As shown in Figure 2a, the as-deposited nanoparticle precursor film was mainly composed of hexagonal Cu_2In ($P6_3/mmc$) and monoclinic CuIn ($P2_1/m$) phases. The CIP treatment did not alter the crystallographic features of the precursor film. However, CIP did induce noticeable changes in the film morphologies; the CIP-treated precursor films had a uniformly higher density compared to films that had not been CIP-treated (control sample, henceforth). Figure 2b reveals that the two-dimensional porosity, ϕ_{2d}, of the film surface was considerably reduced by CIP. Concurrently, the film thickness, l, was found to decrease from 2.2 ± 0.3 to 1.7 ± 0.2 μm, as shown in Figure 2c, which corresponds to an increase in the film density by as much as 23% according to $\rho_b = W/V_{tot} = W/lA$. Here, ρ_b, W, V_{tot}, and A denote the bulk density, the mass of the solid matrix (or substance), the total volume of the thin film including the matrix as well as the open and closed pores, and the surface area of the thin film, respectively.[38] The increase in the film density correlates to the reduced porosity, ϕ, as $\rho_r = \rho_b/\rho_{th} = 1 - \phi$, where ρ_r and ρ_{th} are the relative and theoretical densities of the film, respectively. The improvement in the packing density (relative density) of the precursor film upon CIP treatment is evident in the focused-ion-beam (FIB) cross-sectional images shown in Figure 3. One can see that the average size of the closed pores (represented in black) was smaller in the CIP-treated precursor film. The porosity of the films was estimated to be ϕ = 0.27 ± 0.02 (ρ_r = 0.73) for the

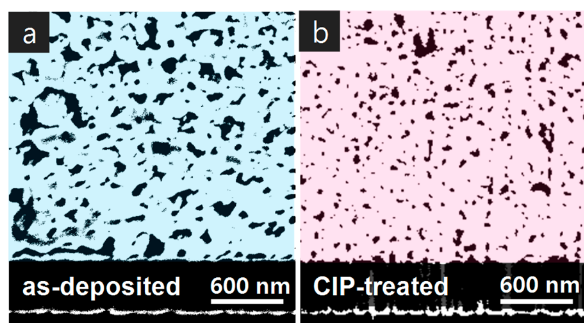

Figure 3. FIB cross sections investigated by FE-SEM for (a) the as-deposited film and (b) the CIP-treated film. Note that the original images were converted to binary images using the specified threshold level with an image analyzer so that the closed pores are represented in black.

control sample and $\phi = 0.14 \pm 0.01$ ($\rho_r = 0.86$) for the CIP-treated film using an image analyzer.

We note here that the concentration ratios of Cu to In, that is, [Cu]/[In], in the Cu−In alloy precursor films were 0.79 ± 0.02 and 0.81 ± 0.02 for the as-deposited and CIP-treated films, respectively. This was analyzed by EDS, as shown in Figure 2b, demonstrating the excellent controllability of the film composition by regulating the mixing ratio of the raw materials (CuCl and $InCl_3$).

The reactive annealing of the Cu−In alloy precursor films at 500 °C for 30 min in the presence of Se vapor induced their phase transformation to ternary chalcogenides and grain growth. The XRD patterns in Figure 4a revealed that the precursor film without CIP treatment (control sample) and the CIP-treated film were completely converted to α-CISe with a chalcopyrite structure (JCPDS No. 87-2265). Raman spectroscopy also indicated the formation of phase-pure α-CISe (Figure S3 in the SI) because the spectra exhibited only an intense peak for the A_1 vibrational mode and weak peaks for the B_2/E modes of chalcopyrite CISe.[39] No trace amounts of secondary phases such as ordered defect compounds or Cu_xSe were detected within the detection limit of the instrument. Upon comparison of two films, one can recognize that the CIP treatment resulted in an overall increase in the diffraction intensity, suggesting enhanced crystallinity and/or increased thickness of the crystalline layer.

Parts b−d of Figure 4 compare the cross sections and surface morphologies of the CISe films prepared by selenization of the as-deposited film with those prepared from the CIP-treated film. It can be recognized that the Mo substrate for the sample without CIP (Figure 4b1) became much thicker after selenization compared to that for the CIP-treated film, which can be attributed to the volume expansion associated with $MoSe_2$ formation. The thicker $MoSe_2$ layer for the control sample is considered to be a consequence of higher Se supply to the Mo surface because of the higher porosity of the precursor film. As shown in Figure 4b, both samples exhibited a typical layered structure,[17,21,34,40−42] that is, a top layer having well-developed grains on a mesoporous bottom layer. On the basis of the depth profile measurement, the compositional unmixing (faster diffusion of Cu toward the surface) during selenization was proposed to be the origin of the formation of this bilayer structure.[34] Namely, preferential grain growth of the upper layer could be induced by Cu enrichment near the surface region, possibly because of the different diffusivities of

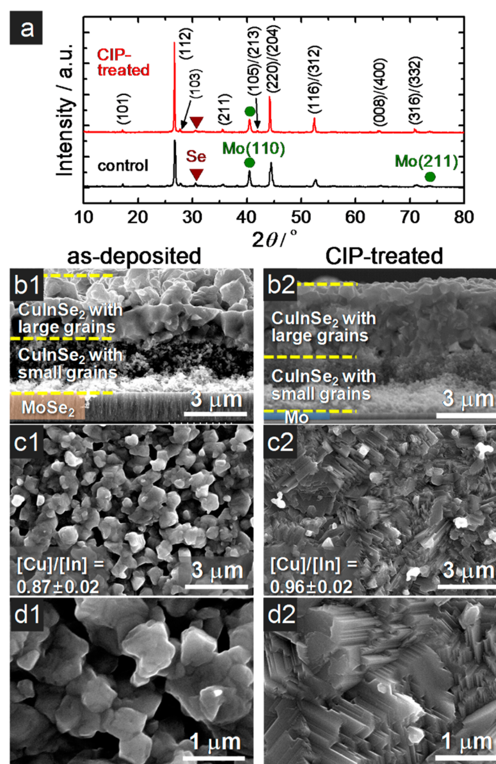

Figure 4. (a) XRD pattern and (b−d) typical SEM images of CISe thin films prepared by selenization of the as-deposited film (left) and the CIP-treated film (right). (b) Cross sections and surface morphologies with (c) lower magnification and (d) higher magnification.

the Cu and In ions in CISe under a chemical potential gradient of Se. In comparison with the control sample, the upper layer in the CIP-treated film was found to be slightly thicker, which is consistent with the higher intensity of the XRD peaks for the CIP-treated film (see also the depth profile analysis in Figure S4 in the SI). The Cu enrichment near the surface region was observed in both films but was more pronounced in the CIP-treated film, as indicated by EDS measurement; the [Cu]/[In] ratio increased from 0.79 to 0.87 for the control sample and from 0.81 to 0.96 for the CIP-treated sample, as shown in Figure 4c. This higher degree of cation unmixing is also in accordance with stronger XRD reflections and a thicker upper layer of the CIP-treated film. It should be noted that the CIP-treated sample also has a more uniform and flat surface (Figure 4b). On the other hand, a more distinct contrast between the two samples could be recognized in the surface morphologies as shown in Figure 4c,d. One can see that the control CISe film has high porosity at the surface, whereas the CIP-treated CISe film exhibited a highly dense surface morphology. Sintering (densification of particle compacts) is driven by matter transport across and/or along the interfaces between contacting particles. It is well-known that increasing the particle-packing density is one of the most effective ways to improve the sintered density in ceramic processing.[43] This idea was demonstrated in solution-processed thin films, as shown in Figure 4. Finally, it is noteworthy that the CIP-treated sample had a well-faceted grain structure, as seen in the higher magnification image (Figure 4d2).

The control and CIP-treated CISe films were integrated into solar cells with a chemically deposited CdS buffer layer and

sputtered i-ZnO and AZO window layers. Note that both devices were fabricated by employing the same batch colloidal solution, heat treatment, and buffer/window layer deposition processes, with the only difference being CIP treatment before selenization of the precursor film. Figure 5 shows the typical PV performances of the resulting solar cells: the current density–voltage ($j-V$) curves under simulated solar illumination (100 mW cm^{-2}, AM 1.5G) and in the dark and the EQEs (η_Q) without bias light. In the $j-V$ characteristics, one can recognize a dramatic improvement in the PV performance of the CIP-treated device compared to the control device. The CIP-treated device exhibited an active area PCE (η) of 8.33% (having a mean value of $\langle\eta\rangle = 8.2 \pm 0.4\%$ with the best efficiency of 9.02%; see Figure S5 in the SI), while the control device showed an active area η of 2.92% (having a mean value of 3.0 ± 0.2% with the best efficiency of 3.28%). The detailed PV parameters for both devices are summarized in Table 1. Among the extracted parameters, the most obvious improvements upon CIP treatment were observed in the values of V_{OC} (by 56% from 0.265 to 0.413 V) and FF (by 62% from 0.34 to 0.55). In comparison, enhancement of the short-circuit current density (j_{SC}) was less pronounced.

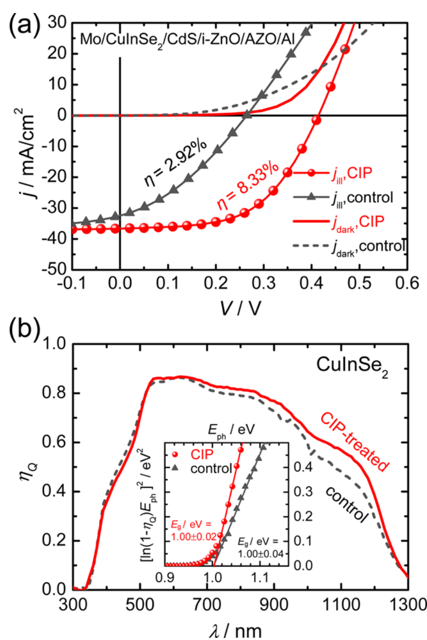

Figure 5. Typical PV performance of the CISe thin film solar cells with and without CIP treatment: (a) $j-V$ characteristics under AM 1.5G illumination and in the dark; (b) EQEs, η_Q, without bias light under short-circuit conditions. Inset in part b: $[\ln(1 - \eta_Q)E_{ph}]^2$ vs E_{ph} curves near the band-edge regime for estimating the band-gap energies of the CISe films.

A closer look at the j_{SC} distribution as a function of the wavelength (λ) of incident light in the EQE spectra (Figure 5b) revealed that most of the enhanced photocurrent by CIP originates in the long-wavelength regime, in particular, in the range of 1000–1200 nm. The absolute values of EQE at around 620 nm were 0.87 for both devices. However, at 1100 nm, it dropped to 0.48 for the control device and to 0.57 for the CIP-treated device. This enhancement of EQEs of the CIP-treated device at the long wavelength (by 19%), namely, its higher collection efficiency, is possibly attributed to the smaller series resistance and/or lower recombination rate because of reduced intergranular interfaces and particle surfaces in the porous bottom layer of the CISe film, as shown in Figure 4. Despite this considerable enhancement in EQEs, the minority carrier collection efficiency still needs to be improved (see the ratio of EQEs at an applied bias of −1 V to that at 0 V in Figure S6 in the SI). A better collection efficiency, particularly deep in the absorber layer, may be achieved by a homogeneous microstructure throughout the absorber layer. Accordingly, further work is in progress to suppress the formation of a bilayer structure in CISe thin films. The band-gap energies were estimated by linear regression on the plot of $[\ln(1 - \eta_Q)E_{ph}]^2$ versus photon energy, E_{ph}, as depicted in the inset of Figure 5b. The results show that the control and CIP-treated CISe thin films have almost identical band-gap energies, 1.0 eV, which is slightly smaller than the reported value for a single crystal, 1.04 eV.[44]

4. DISCUSSION

In order to gain more insight into the origin of the different PV performances, in particular V_{OC} and FF, between the control and CIP-treated devices, we analyzed the diode curves in the dark based on the following equation:[34,45]

$$j_d = j_0\left[\exp\left(\frac{e(V - j_d R_s)}{nkT}\right) - 1\right] + G_{sh}V \quad (1)$$

where j_d, j_0, e, k, n, R_s, and G_{sh} denote the diode current density, reverse saturation current density, elementary electron charge, Boltzmann constant, diode ideality factor, area-normalized series resistance, and area-normalized shunt conductance, respectively. Figure 6 depicts the procedure to evaluate the PV parameters (G_{sh}, R_s, n, and j_0) using a standard diode analysis: (a) plot of dj/dV versus V, where the shunt conductance, G_{sh}, was evaluated from the constant dj/dV values in the range of $V \leq 0$, provided that a linear shunt current predominates the diode current where $V \leq 0$; (b) plot of dV/dj versus $1/(j - G_{sh}V)$, where R_s and n were estimated from the y intercept and the slope in the high bias regime; (c) plot of $\ln(j - G_{sh}V)$ versus $V - jR_s$, where j_0 and n were extracted from the y intercept and slope. Note that the ideality factor, n, is determined in Figure 6b,c, respectively, and therefore their mutual agreement may be used as a measure of the validity of the above analysis. The resulting PV parameters

Table 1. Comparison of Typical PV Parameters along with the Mean Values of Power Conversion Efficiencies, $\langle\eta\rangle$, Evaluated from the $j-V$ Curves under AM 1.5G Illumination and EQE Spectra for CISe Solar Cells with and without CIP Treatment

CISe	V_{OC}/V	j_{SC}/mA cm^{-2}	FF	A_{ac}/cm^2	η^a/%	$\langle\eta\rangle$/%	E_g/eV	$E_g/e - V_{OC}$/V
control	0.265	32.4	0.34	0.35	2.92	3.0 ± 0.2(8)^b	1.00	0.735
CIP-treated	0.413	36.6	0.55	0.33	8.33	8.2 ± 0.4(7)	1.00	0.587

^{a}Each measured without antireflection coating and calculated with respect to the active area, A_{ac}. ^{b}The numerals in parentheses represent the number of PV cells on a substrate (3 × 4 cm^2) with which the mean values for efficiency, $\langle\eta\rangle$, were evaluated, excluding a shunted device.

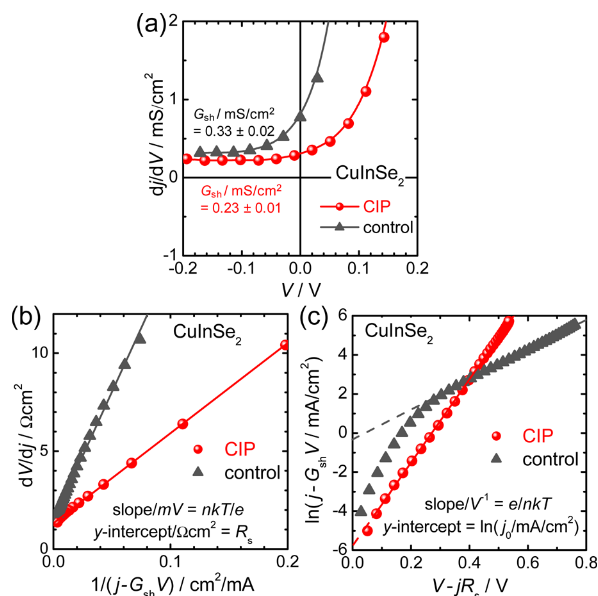

Figure 6. Diode analysis on CISe solar cells with and without CIP treatment: (a) dj/dV vs V curves for G_{sh} evaluation; (b) dV/dj vs $1/(j - G_{sh}V)$ plot for determination of R_s and n; (c) semilogarithmic plot of $(j - G_{sh}V)$ vs $V - jR_s$ for determination of n and j_0.

are summarized in Table 2, where the ideality factor, n, represents the average value obtained from Figure 6b,c.

It is not surprising that the CIP-treated device had a lower shunt conductance (G_{sh}) and series resistance (R_s) in view of the microstrucural improvement induced by CIP treatment. It is suggested that a better developed microstructure, i.e., less porosity, reduced grain boundaries, and thinner $MoSe_2$ layer, in the CIP-treated CISe consequently resulted in the reduction of G_{sh} and R_s by 30% and 11%, respectively.

However, among the PV parameters in Table 2, more pronounced changes can be found in the saturation current density (j_0) and ideality factor (n). The j_0 value for the CIP-treated device was smaller, by more than 2 orders of magnitude, compared to that of the control device. The remarkable enhancement of V_{OC} for the CIP-treated device (Figure 5) could be attributed to this markedly reduced j_0 according to[46]

$$V_{OC} \approx \frac{nkT}{e} \ln\left(\frac{j_{SC}}{j_0}\right) \qquad \text{with} \qquad j_0 = j_{00} \exp\left(-\frac{E_a}{nkT}\right) \tag{2}$$

Here, j_{00} and E_a are the preexponential factor and activation energy of the saturation current density, respectively. The saturation current is a measure of recombination in a $p-n$ junction diode.[47] Namely, the lower j_0 value for the CIP-treated device indicates a smaller amount of recombination compared to the control device. This could be ascribed to the reduced number of defects at internal interfaces in the porous bottom layer (e.g., at pore surfaces or grain boundaries) as well as to the reduced number of defects around the CISe surface, which is associated with the enhanced planarity and reduced porosity at the CISe/CdS junction (Figure 4).

In Figure 7a, the j_0 values of the devices used in the present study are compared with the reported[47] and theoretical values.

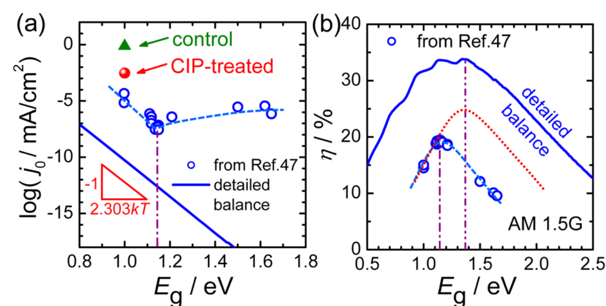

Figure 7. PV parameters for $Cu(In_{1-x}Ga_x)Se_2$ solar cells as a function of E_g: (a) reverse saturation current density, j_0; (b) PCE, η.

The reverse saturation current density for an ideal homojunction diode is given as[48]

$$j_0 = eN_CN_V\left(\sqrt{\frac{D_n}{\tau_n}}\frac{1}{N_A} + \sqrt{\frac{D_p}{\tau_p}}\frac{1}{N_D}\right)\exp\left(-\frac{E_g}{kT}\right) \tag{3}$$

where N_C and N_V stand for the effective density of states in the conduction and valence bands, N_A and N_D the acceptor and donor concentrations, D_n and D_p the diffusion coefficients, and τ_n and τ_p the minority carrier lifetimes for electrons and holes, respectively. The minimum possible j_0 values for an ideal solar cell, in which only radiative recombination takes place in the neutral region, can be estimated by using the principle of detailed balance.[49] The results are depicted by a solid line in Figure 7a. The calculated j_0 values are linearly dependent on the band-gap energy (E_g) on the semilogarithmic scale. The slope in the plot of log j_0 versus E_g was found to be $-1/2.303kT$, which is in agreement with eq 3. According to the detailed balance calculation, the band gap of the solar cell absorber should be in the range of 1.37−1.40 eV for the maximum theoretical PCE, as represented by a solid curve in Figure 7b. In practice, however, it has been empirically known that the highest efficiency of $Cu(In_{1-x}Ga_x)Se_2$ (CIGS) solar cells fabricated by a coevaporation method could be achieved when the band gap of the CIGS absorber was around 1.15 eV (open circle in Figure 7b).[47] This discrepancy between the theoretically and experimentally determined values is primarily attributed to the abnormal behavior of the empirical values for j_0 in the range of $E_g > 1.15$ eV (open circle in Figure 7a):[47] The measured and theoretical values for j_0 seem to have the same E_g dependence in the range of $E_g < 1.15$ eV. However, a further increase in E_g resulted in the inverse dependence of j_0 on E_g. This undesirable increase of j_0 with increasing E_g above 1.15 eV eventually brings about the lower V_{OC} according to eq 2 and

Table 2. Area-Normalized Shunt Conductance (G_{sh}) and Series Resistance (R_s), Ideality Factor (n), and Reverse Saturation Current Density (j_0) of CISe Devices with and without CIP Treatment

CISe	G_{sh}/mS cm^{-2}	R_s/Ω cm^2	n	j_0/mA cm^{-2}
control	0.33 ± 0.02	1.49 ± 0.04	5.10 ± 0.08 (5.10 and 5.10)[a]	(7.4 ± 0.1) × 10^{-1}
CIP-treated	0.23 ± 0.01	1.32 ± 0.01	1.82 ± 0.05 (1.81 and 1.83)	(3.0 ± 0.1) × 10^{-3}

[a]Both n values in parentheses are evaluated from Figure 6b,c, respectively.

thereby a lower efficiency than would be expected (dotted curve in Figure 7b). In brief, the CIGS solar cell with the highest efficiency, 19.5% at E_g = 1.15 eV, exhibited the lowest j_0 value, as shown in Figure 7.[47] The above discussion emphasizes the significance of j_0 as a determinant of V_{OC} and thereby the PCE of a solar cell. We ascertained that the enhanced V_{OC} and PCE of the present device upon CIP treatment were also accompanied by a largely reduced j_0. However, compared to the reported value for the vacuum-deposited CISe with a comparable band gap, the present j_0 value (3×10^{-3} mA cm^{-2}) is still higher by ca. 2 orders of magnitude, as shown in Figure 7a, which implies that the j_0 value can be reduced further by morphological and/or defect-chemical modification of the absorber as well as the $p-n$ junction.

To elucidate the dominant recombination mechanism of the present devices that determines the magnitude of j_0 and thereby the deficiency in V_{OC} ($E_g/e - V_{OC}$ in Table 1), we investigated the temperature (T) dependence of V_{OC} for both devices, as shown in Figure 8. The $j-V$ characteristics as a function of T

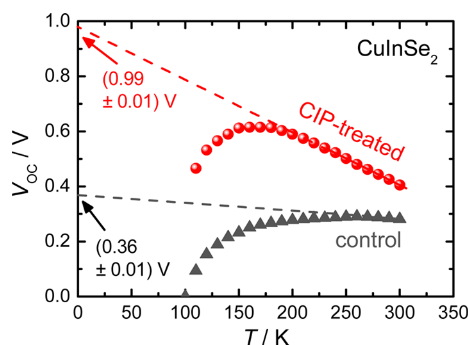

Figure 8. Open-circuit voltage (V_{OC}) of CISe solar cells as a function of the temperature. Note that the linear extrapolation to 0 K depicted by the dashed line indicates the activation energy (E_a) of the dominant recombination mechanism.

under 1-sun-equivalent solar illumination are presented in Figure S7 in the SI. By rearrangement of eq 2, V_{OC} can be expressed as follows:

$$V_{OC} \approx \frac{E_a}{e} - \frac{nkT}{e}\ln\left(\frac{j_{00}}{j_{SC}}\right) \quad (4)$$

Equation 4 enables us to extract the activation energy of the predominant recombination process, E_a: With the y intercept at T = 0, extrapolated from the V_{OC} versus T plot in the high-T linear regime,[50] we obtained E_a = 0.99 ± 0.01 eV for the CIP-treated device and E_a = 0.36 ± 0.01 eV for the control device. The former agreed well with the band-gap energy (E_g = 1.0 eV) evaluated from the EQE measurement, while the latter was much lower than E_g. The E_a value being close to E_g for the CIP-treated device indicates that the dominant recombination current originates from the CISe absorber layer.[51] On the contrary, the significantly lower E_a value than E_g would suggest, in general, that the recombination current is strongly augmented by interface recombination, which results in higher values for j_0 and $E_g/e - V_{OC}$. This argument can be related with the microstructural features in Figure 4; the highly porous and rough surface of the control CISe thin film could cause a defective absorber/buffer interface and hence lead to high interface recombination. On the other hand, the effect of different [Cu]/[In] ratios of the two sintered films on the interface recombination is not clear with the limited data of the present work. It should be pointed out, however, that the above discussion could not explain all possible origins for the lower E_a value for the control device because j_{SC} also began to decrease at room temperature as T decreased (Figure S7 in the SI).

Finally, we consider the diode ideality factor, n, as another indicator of the dominant recombination mechanism. An n value of unity corresponds to the ideal diode in which the recombination occurs only in the neutral region (either via band-to-band or via intra-band-gap defect states), with no recombination occurring in the depletion or space charge region (SCR). When the SCR recombination becomes predominant, the n value tends to be closer to 2. An n value higher than 2 indicates additional contributions to the total recombination, such as interface recombination and tunneling-enhanced recombination in the SCR or at the interfaces.[46,52] The present value for the control device (n = 5.1) possibly implies that this device suffers from a large amount of tunneling-enhanced SCR and/or interface recombination. However, CIP treatment significantly reduced the n value down to 1.82. This n value that is close to 2, in conjunction with the fact that $E_a = E_g$ (Figure 8), indicates that the defect-related (Schottky−Read−Hall, SRH) recombination dominates in the SCR of the CIP-treated device.[50]

We have shown that the enhancement of V_{OC} and PCE for the CIP-treated device is associated with the reduced j_0 and n values. On the other hand, the increase in the j_0 and n values has been known to significantly reduce FF as well.[53] Therefore, the reduced j_0 and n values, aside from the lower G_{sh} and R_s, of the CIP-treated device can be regarded as the origin of the enhanced FF.

5. CONCLUSIONS

The influence of the green density of the Cu−In nanoparticle precursor film on the PV performance of CISe solar cells was examined with the composition variable fixed as [Cu]/[In] ≈ 0.8. The CIP increased the relative density of the precursor film by ca. 20%. As a result, the CISe thin films with CIP treatment exhibited morphological features quite distinct from those of the control thin films: a thicker top crystalline layer, a highly dense microstructure in the upper layer, a possibly increased packing density of the bottom layer, a more uniform and flat surface, and a thinner $MoSe_2$ layer. These microstructural improvements by CIP resulted in an almost 3-fold increase in the average PCE for the resulting low-band-gap (1.0 eV) CISe PV devices compared to the control devices (from 3.0 to 8.2% with the highest value of 9.02%). The better minority carrier collection efficiency, particularly in the wavelength range of 1000−1200 nm, gave rise to the enhanced j_{SC} for the CIP device by ca. 13%. However, more decisive PV parameters for the markedly increased η were V_{OC} and FF, which improved by ca. 60%.

Analysis of the diode $j-V$ curves revealed that the reduction in G_{sh} (by 30%) and R_s (by 11%) was evident in the CIP device but was less pronounced than the reduction in j_0 (by more than 2 orders of magnitude) and n (by 65%). The n value of 1.82 together with an E_a value that is equal to E_g for the CIP-treated device suggested that the SRH recombination is the predominant process. In contrast, the n value that was much higher than 2, along with the fact that $E_a < E_g$ for the control device, implied that an additional contribution such as interface recombination and/or tunneling-enhanced recombination may prevail. In this regard, the lower j_0 and n values (suppression of

the recombination current) in the CIP-treated device could be attributed to the reduced number of defects at the internal interfaces such as pore surfaces and grain boundaries in the porous bottom layer as well as to the reduced number of defects near the CISe surface having enhanced flatness and planar density.

In summary, an increase in the relative density of the precursor film had a great influence on the microstructural development of CISe films, leading to reduction of the parasitic resistances and more significantly to suppression of the recombination current, which eventually resulted in the remarkable enhancement in V_{OC}, FF, and η. Finally, we point out that the present approach can be extended to other kinds of solid-state devices employing solution-based deposition such as thin-film solar cells based on various compositions of chalcogenides, quantum-dot solar cells, organic−inorganic hybrid solar cells, transparent conducting oxide electrodes, supercapacitors, solid oxide fuel cells, etc.

■ ASSOCIATED CONTENT

Ⓢ Supporting Information

TEM image of as-synthesized Cu−In nanoparticles, SEM image of the precursor film compressed by uniaxial pressing, Raman spectra of CISe thin films, relative diffraction intensity of (112) and (220)/(224) planes for CISe, relative atomic composition depth profiles measured by AES, ratio of EQEs at an applied potential of −1 V with respect to that at 0 V, and j−V characteristics as a function of the temperature. This material is available free of charge via the Internet at http://pubs.acs.org.

■ AUTHOR INFORMATION

Corresponding Author

*Tel: +82-2-958-6710. Fax: +82-2-958-6649. E-mail: dklee@kist.re.kr.

Notes

The authors declare no competing financial interest.

■ ACKNOWLEDGMENTS

This work was supported by the program of KIST and the "National Agenda Project" program of Korea Research Council of Fundamental Science & Technology. Also, the authors acknowledge support by the KUUC program.

■ REFERENCES

(1) Lange, F. F. *Science* **1996**, *273*, 903−909.
(2) Jia, Q. X.; McCleskey, T. M.; Burrell, A. K.; Lin, Y.; Collis, G. E.; Wang, H.; Li, A. D. Q.; Foltyn, S. R. *Nat. Mater.* **2004**, *3*, 529−532.
(3) Habas, S. E.; Platt, H. A. S.; van Hest, M. F. A. M.; Ginley, D. S. *Chem. Rev.* **2010**, *110*, 6571−6594.
(4) Jasieniak, J.; MacDonald, B. I.; Watkins, S. E.; Mulvaney, P. *Nano Lett.* **2011**, *11*, 2856−2864.
(5) Rath, A. K.; Bernechea, M.; Martinez, L.; de Arquer, F. P. G.; Osmond, J.; Konstantatos, G. *Nat. Photonics* **2012**, *6*, 529−534.
(6) Kevin, M.; Lee, G. H.; Ho, G. W. *Energy Environ. Sci.* **2012**, *5*, 7196−7202.
(7) Gutiérrez, J.; Llordés, A.; Gázquez, J.; Gibert, M.; Romà, N.; Ricart, S.; Pomar, A.; Sandiumenge, F.; Mestres, N.; Puig, T.; Obradors, X. *Nat. Mater.* **2007**, *6*, 367−373.
(8) Oh, E.-O.; Whang, C.-M.; Lee, Y.-R.; Park, S.-Y.; Prasad, D. H.; Yoon, K.-J.; Son, J.-W.; Lee, J.-H.; Lee, H.-W. *Adv. Mater.* **2012**, *24*, 3373−3377.
(9) Guillemoles, J.-F.; Kronik, L.; Cahen, D.; Rau, U.; Jasenek, A.; Schock, H.-W. *J. Phys. Chem. B* **2000**, *104*, 4849−4862.
(10) Chirilă, A.; Reinhard, P.; Pianezzi, F.; Bloesch, P.; Uhl, A. R.; Fella, C.; Kranz, L.; Keller, D.; Gretener, C.; Hagendorfer, H.; Jaeger, D.; Erni, R.; Nishiwaki, S.; Buecheler, S.; Tiwari, A. N. *Nat. Mater.* **2013**, *12*, 1107−1111.
(11) Hibberd, C. J.; Chassaing, E.; Liu, W.; Mitzi, D. B.; Lincot, D.; Tiwari, A. N. *Prog. Photovoltaics* **2010**, *18*, 434−452.
(12) Lincot, D.; Guillemoles, J.-F.; Taunier, S.; Guimard, D.; Sicx-Kurdi, J.; Chaumont, A.; Roussel, O.; Grand, P.-P.; Benfarah, M.; Mogensen, P.; Kerrec, O. *Sol. Energy* **2004**, *77*, 725−737.
(13) Lee, H.; Lee, W.; Kim, J. Y.; Ko, M. J.; Kim, K.; Seo, K.; Lee, D.-K.; Kim, H. *Electrochim. Acta* **2013**, *87*, 450−456.
(14) Bhattacharya, R. N.; Hiltner, J. F.; Batchelor, W.; Contreras, M. A.; Noufi, R. N.; Sites, J. R. *Thin Solid Films* **2000**, *361*−*362*, 396−399.
(15) Guo, Q.; Ford, G. M.; Agrawal, R.; Hillhouse, H. W. *Prog. Photovoltaics* **2013**, *21*, 64−71.
(16) Brown, G.; Stone, P.; Woodruff, J.; Cardozo, B.; Jackrel, D. *Conf. Rec. IEEE Photovoltaic Spec. Conf.* **2012**, 3230−3233.
(17) Norsworthy, G.; Leidholm, C. R.; Halani, A.; Kapur, V. K.; Roe, R.; Basol, B. M.; Matson, R. *Sol. Energy Mater. Sol. Cells* **2000**, *60*, 127−134.
(18) Panthani, M. G.; Akhavan, V.; Goodfellow, B.; Schmidtke, J. P.; Dunn, L.; Dodabalapur, A.; Barbara, P. F.; Korgel, B. A. *J. Am. Chem. Soc.* **2008**, *130*, 16770−16777.
(19) Akhavan, V. A.; Goodfellow, B. W.; Panthani, M. G.; Reid, D. K.; Hellebusch, D. J.; Adachi, T.; Korgel, B. A. *Energy Environ. Sci.* **2010**, *3*, 1600−1606.
(20) Chang, S.-H.; Chiang, M.-Y.; Chiang, C.-C.; Yuan, F.-W.; Chen, C.-Y.; Chiu, B.-C.; Kao, T.-L.; Lai, C.-H.; Tuan, H.-Y. *Energy Environ. Sci.* **2011**, *4*, 4929−4932.
(21) Kind, C.; Feldmann, C.; Quintilla, A.; Ahlswede, E. *Chem. Mater.* **2011**, *23*, 5269−5274.
(22) Jeong, S.; Lee, B.-S.; Ahn, S.; Yoon, K.; Seo, Y.-H.; Choi, Y.; Ryu, B.-H. *Energy Environ. Sci.* **2012**, *5*, 7539−7542.
(23) Todorov, T. K.; Gunawan, O.; Gokmen, T.; Mitzi, D. B. *Prog. Photovoltaics* **2013**, *21*, 82−87.
(24) Kaelin, M.; Rudmann, D.; Kurdesau, F.; Zogg, H.; Meyer, T.; Tiwari, A. N. *Thin Solid Films* **2005**, *480*−*481*, 486−490.
(25) Li, L.; Coates, N.; Moses, D. *J. Am. Chem. Soc.* **2010**, *132*, 22−23.
(26) Weil, B. D.; Connor, S. T.; Cui, Y. *J. Am. Chem. Soc.* **2010**, *132*, 6642−6643.
(27) Lee, E.; Park, S. J.; Cho, J. W.; Gwak, J.; Oh, M.-K.; Min, B. K. *Sol. Energy Mater. Sol. Cells* **2011**, *95*, 2928−2932.
(28) Uhl, A. R.; Fella, C.; Chirila, A.; Kaelin, M. R.; Karvonen, L.; Weidenkaff, A.; Borca, C. N.; Grolimund, D.; Romanyuk, Y. E.; Tiwari, A. N. *Prog. Photovoltaics* **2012**, *20*, 526−533.
(29) Wang, G.; Wang, S.; Cui, Y.; Pan, D. *Chem. Mater.* **2012**, *24*, 3993−3997.
(30) Ahn, S.; Son, T. H.; Cho, A.; Gwak, J.; Yun, J. H.; Shin, K.; Ahn, S. K.; Park, S. H.; Yoon, K. *ChemSusChem* **2012**, *5*, 1773−1777.
(31) Todorov, T. K.; Reuter, K. B.; Mitzi, D. B. *Adv. Mater.* **2010**, *22*, E156−E159.
(32) Cho, A.; Ahn, S.; Yun, J. H.; Gwak, J.; Song, H.; Yoon, K. *J. Mater. Chem.* **2012**, *22*, 17893−17899.
(33) Cai, Y.; Ho, J. C. W.; Batabyal, S. K.; Liu, W.; Sun, Y.; Mhaisalkar, S. G.; Wong, L. H. *ACS Appl. Mater. Interfaces* **2013**, *5*, 1533−1537.
(34) Lim, Y. S.; Jeong, J.; Kim, J. Y.; Ko, M. J.; Kim, H.; Kim, B.; Jeong, U.; Lee, D.-K. *J. Phys. Chem. C* **2013**, *117*, 11930−11940.
(35) Eldada, L.; Peter, H.; Stanbery, B. J. *Proc. SPIE* **2010**, *7771*, 77710I-1−77770I-14.
(36) Hsiao, L. Y.; Duh, J. G. *J. Electrochem. Soc.* **2005**, *152*, J105−J109.
(37) Brooks, L. S. *J. Am. Chem. Soc.* **1952**, *74*, 227−229.
(38) Griffiths, R.; Radford, C. *Calculations in Ceramics*; Maclaren and Sons Ltd.: London, 1965; p 28.
(39) Tanino, H.; Maeda, T.; Fujikake, H.; Nakanishi, H.; Endo, S.; Irie, T. *Phys. Rev. B* **1992**, *45*, 13323−13330.

(40) Guo, Q.; Ford, G. M.; Hillhouse, H. W.; Agrawal, R. *Nano Lett.* **2009**, *9*, 3060−3065.
(41) Chen, G.; Wang, L.; Sheng, X.; Yang, D. *J. Mater. Sci.: Mater. Electron.* **2011**, *22*, 1124−1129.
(42) Liu, C. P.; Chuang, C. L. *Sol. Energy* **2012**, *86*, 2795−2801.
(43) Barringer, E. A.; Bowen, H. K. *Appl. Phys. A* **1988**, *45*, 271−275.
(44) Shay, J. L.; Tell, B.; Kasper, H. M.; Schiavone, L. M. *Phys. Rev. B* **1973**, *7*, 4485−4490.
(45) Sites, J. R.; Mauk, P. H. *Sol. Cells* **1989**, *27*, 411−417.
(46) Rau, U.; Schock, H. W. *Appl. Phys. A* **1999**, *69*, 131−147.
(47) Contreras, M. A.; Ramanathan, K.; AbuShama, J.; Hasoon, F.; Young, D. L.; Egaas, B.; Noufi, R. *Prog. Photovoltaics* **2005**, *13*, 209−216.
(48) Neudeck, G. W. *The PN Junction Diode*, 2nd ed.; Addison-Wesley Publishing Co.: Reading, MA, 1989; p 65.
(49) Shockley, W.; Queisser, H. J. *J. Appl. Phys.* **1961**, *32*, 510−519.
(50) Nadenau, V.; Rau, U.; Jasenek, A.; Schock, H. W. *J. Appl. Phys.* **2000**, *87*, 584−593.
(51) Hegedus, S. S.; Shafarman, W. N. *Prog. Photovoltaics* **2004**, *12*, 155−176.
(52) Rau, U. *Appl. Phys. Lett.* **1999**, *74*, 111−113.
(53) Zhu, K.; Jang, S. R.; Frank, A. J. *J. Phys. Chem. Lett.* **2011**, *2*, 1070−1076.

dx.doi.org/10.1021/am4040976 | *ACS Appl. Mater. Interfaces* 2014, 6, 259−267